THE ASTROPHYSICAL JOURNAL, 790:12 (16pp), 2014 July 20

doi:10.1088/0004-637X/790/1/12

© 2014. The American Astronomical Society. All rights reserved. Printed in the U.S.A.

KEPLER-93b: A TERRESTRIAL WORLD MEASURED TO WITHIN 120 km, AND A TEST CASE FOR A NEW *SPITZER* OBSERVING MODE

SARAH BALLARD[1,16], WILLIAM J. CHAPLIN[2,3], DAVID CHARBONNEAU[4], JEAN-MICHEL DÉSERT[5], FRANCOIS FRESSIN[4], LI ZENG[4],
MICHAEL W. WERNER[6], GUY R. DAVIES[2,3], VICTOR SILVA AGUIRRE[3], SARBANI BASU[7], JØRGEN CHRISTENSEN-DALSGAARD[3],
TRAVIS S. METCALFE[3,8], DENNIS STELLO[9], TIMOTHY R. BEDDING[9], TIAGO L. CAMPANTE[2,3], RASMUS HANDBERG[2,3],
CHRISTOFFER KAROFF[3], YVONNE ELSWORTH[2,3], RONALD L. GILLILAND[10], SASKIA HEKKER[2,11,12], DANIEL HUBER[13,14],
STEVEN D. KAWALER[15], HANS KJELDSEN[3], MIKKEL N. LUND[3], AND MIA LUNDKVIST[3]
[1] University of Washington, Seattle, WA 98195, USA; sarahba@uw.edu
[2] School of Physics and Astronomy, University of Birmingham, Edgbaston, Birmingham, B15 2TT, UK
[3] Stellar Astrophysics Centre (SAC), Department of Physics and Astronomy, Aarhus University, Ny Munkegade 120, DK-8000 Aarhus C, Denmark
[4] Harvard-Smithsonian Center for Astrophysics, Cambridge, MA 02138, USA
[5] Department of Astrophysical and Planetary Sciences, University of Colorado, Boulder CO 80309, USA
[6] Jet Propulsion Laboratory, California Institute of Technology, Pasadena, CA 91125, USA
[7] Department of Astronomy, Yale University, New Haven, CT 06520, USA
[8] Space Science Institute, Boulder, CO 80301, USA
[9] Sydney Institute for Astronomy, School of Physics, University of Sydney 2006, Australia
[10] Center for Exoplanets and Habitable Worlds, The Pennsylvania State University, University Park, PA 16802, USA
[11] Max-Planck-Institut für Sonnensystemforschung, Justus-von-Liebig-Weg 3, D-37077 Göttingen, Germany
[12] Astronomical Institute, "Anton Pannekoek," University of Amsterdam, The Netherlands
[13] NASA Ames Research Center, Moffett Field, CA 94035, USA
[14] SETI Institute, 189 Bernardo Avenue, Mountain View, CA 94043, USA
[15] Department of Physics and Astronomy, Iowa State University, Ames, IA 50011, USA
Received 2014 January 5; accepted 2014 May 13; published 2014 June 27

ABSTRACT

We present the characterization of the Kepler-93 exoplanetary system, based on three years of photometry gathered by the *Kepler* spacecraft. The duration and cadence of the *Kepler* observations, in tandem with the brightness of the star, enable unusually precise constraints on both the planet and its host. We conduct an asteroseismic analysis of the *Kepler* photometry and conclude that the star has an average density of 1.652 ± 0.006 g cm^{-3}. Its mass of $0.911 \pm 0.033\ M_\odot$ renders it one of the lowest-mass subjects of asteroseismic study. An analysis of the transit signature produced by the planet Kepler-93b, which appears with a period of $4.72673978 \pm 9.7 \times 10^{-7}$ days, returns a consistent but less precise measurement of the stellar density, $1.72^{+0.02}_{-0.28}$ g cm^{-3}. The agreement of these two values lends credence to the planetary interpretation of the transit signal. The achromatic transit depth, as compared between *Kepler* and the *Spitzer Space Telescope*, supports the same conclusion. We observed seven transits of Kepler-93b with *Spitzer*, three of which we conducted in a new observing mode. The pointing strategy we employed to gather this subset of observations halved our uncertainty on the transit radius ratio $R_P/R_\star$. We find, after folding together the stellar radius measurement of $0.919 \pm 0.011\ R_\odot$ with the transit depth, a best-fit value for the planetary radius of $1.481 \pm 0.019\ R_\oplus$. The uncertainty of 120 km on our measurement of the planet's size currently renders it one of the most precisely measured planetary radii outside of the solar system. Together with the radius, the planetary mass of $3.8 \pm 1.5\ M_\oplus$ corresponds to a rocky density of 6.3 ± 2.6 g cm^{-3}. After applying a prior on the plausible maximum densities of similarly sized worlds between 1 and $1.5\ R_\oplus$, we find that Kepler-93b possesses an average density within this group.

Key words: eclipses – methods: observational – planetary systems – stars: individual (KOI 69, KIC 3544595)

Online-only material: color figures

1. INTRODUCTION

The number of confirmed exoplanets now stands at 1750 (Lissauer et al. 2014; Rowe et al. 2014). This figure excludes the additional thousands of candidates identified by the *Kepler* spacecraft, which possess a mean false positive rate of 10% (Morton & Johnson 2011; Fressin et al. 2013). The wealth of data from NASA's *Kepler* mission in particular has enabled statistical results on the ubiquity of small exoplanets. Fressin et al. (2013) investigated planet occurrence for stellar spectral types ranging from F to M, while Petigura et al. (2013a, 2013b) focused upon Sunlike stars and both Dressing & Charbonneau (2013) and Swift et al. (2013) on smaller M dwarfs. However,

of the more than 4000 planetary candidates identified by *Kepler*, only 58 possess measured masses.[17] We define a mass measurement to be a detection of the planet with 95% confidence, from either radial velocity (RV) measurements or transit timing variations. The time-intensive nature of follow-up observations renders only a small subsample amenable to such detailed study. Kepler-93, a very bright (*V* magnitude of 10) host star to a rocky planet, is a member of this singular group. It has been the subject of a dedicated campaign of observations spanning the three years since its identification as a candidate (Borucki et al. 2011).

An asteroseismic investigation underpins our understanding of the host star. Asteroseismology, which employs the oscillation

---

[16] NASA Carl Sagan Fellow.

[17] From exoplanets.org, accessed on 2014 March 17.

timescales of stars from their brightness or velocity variations, is a powerful means of probing stellar interiors. Asteroseismic measurements derived from photometry require a long observational baseline at high cadence (to detect typically mHz frequencies) and photometric precision at the level of 10 ppm. Where these measurements are achievable, they constrain stellar densities with a precision of 1% and stellar ages within 10% (Brown & Gilliland 1994; Silva Aguirre et al. 2013). The technique can enrich the studies of transiting exoplanets, whose photometric signature independently probes the stellar density. The ratio of the semi-major axis to the radius of the host star ($a/R_\star$) is a transit observable property, and is directly related to the mean density of the host star (Seager & Mallén-Ornelas 2003, Sozzetti et al. 2007 and Torres et al. 2008). Nutzman et al. (2011) were the first to apply an asteroseismic density measurement of an exoplanet host star, in tandem with a transit light curve, to refine knowledge of the planet. With transit photometry gathered with the Fine Guidance Sensor on the *Hubble Space Telescope*, they employed the asteroseismic solution derived by Gilliland et al. (2011) to constrain their transit fit. This method resulted in a three-fold precision improvement on the radius of HD 17156b ($1.0870 \pm 0.0066\ R_J$ compared to $1.095 \pm 0.020\ R_J$). The *Kepler* mission's long baselines and unprecedented photometric precision make asteroseismic studies of exoplanet hosts possible on large scales. Batalha et al. (2011) used asteroseismic priors on the host star in their study of Kepler's first rocky planet Kepler-10b, recently updated by Fogtmann-Schulz et al. (2014). Asteroseismic characterization of the host star also informed the exoplanetary studies of Howell et al. (2012), Borucki et al. (2012), Carter et al. (2012), Barclay et al. (2013), Chaplin et al. (2013), and Gilliland et al. (2013). Huber et al. (2013) increased the number of *Kepler* exoplanet host stars with asteroseismic solutions to 77. Kepler-93 is a rare example of a sub-solar mass main-sequence dwarf that is bright enough to yield high-quality data for asteroseismology. Intrinsically faint, cool dwarfs show weaker-amplitude oscillations than their more luminous cousins. These targets are scientifically valuable not only as exoplanet hosts, but also as test beds for stellar interior physics in the sub-solar mass regime.

In addition to its science merit as a rocky planet host, the brightness of Kepler-93 made it an optimal test subject for a new observing mode with the *Spitzer Space Telescope*. *Spitzer*, and in particular its Infrared Array Camera (IRAC; Fazio et al. 2004), has a rich history of enhancing exoplanetary studies. Previous studies with IRAC include maps of planetary weather (Knutson et al. 2007), characterization of super-Earth atmospheres (Désert et al. 2011), and the detection of new worlds (Demory et al. 2011). Applications of post-cryogenic *Spitzer* to the *Kepler* planets address in largest part the false-positive hypothesis. An authentic planet will present the same transit depth, independent of the wavelength at which we observe it. Combined with other pieces of evidence, warm *Spitzer* observations at 4.5 μm contributed to the validations of a number of Kepler Objects of Interest (KOIs). These planets include Kepler-10c (Fressin et al. 2011), Kepler-14b (Buchhave et al. 2011), Kepler-18c and d (Cochran et al. 2011), Kepler-19b (Ballard et al. 2011), Kepler-22b (Borucki et al. 2012), Kepler-25b and c (Steffen et al. 2012), Kepler-20c, d, e, and f (Gautier et al. 2012; Fressin et al. 2012), Kepler-61b (Ballard et al. 2013), and Kepler-401b (Van Eylen et al. 2014). The growing list of transiting exoplanets includes ever smaller planets around dimmer stars. *Spitzer* observations of their transits are more challenging as the size of the astrophysical signal approaches the size of instrumental

sources of noise. The Spitzer Science Center developed the "peak-up" observational technique, detailed in Ingalls et al. (2012) and Grillmair et al. (2012), to improve the ultimate precision achievable with IRAC. Kepler-93 had been the subject of *Spitzer* observations prior to these improvements to test the false-positive hypothesis for the system. These pre-existing *Spitzer* observations of the star, combined with the intrinsic brightness of the target (which enables *Spitzer* to peak-up on the science target rather than an adjacent star within an acceptance magnitude range), made Kepler-93b an ideal test subject for the efficacy of peak-up. To this end, *Spitzer* observed a total of seven full transits of Kepler-93b on the same pixel, four without peak-up mode and three with peak-up mode enabled. This data set allows us to investigate the effectiveness of the peak-up pointing strategy for *Spitzer*.

In Section 2, we present our analysis of the *Kepler* transit light curve. We describe our measurement and characterization of the asteroseismic spectrum of the star, as well as the transit parameters. In Section 3, we describe our reduction and analysis of seven *Spitzer* light curves of Kepler-93, and detail the effects of the peak-up observing mode to the photometry. We go on in Section 4 to present evidence for the authentic planetary nature of Kepler-93b. Our reasoning is based on the consistency of the asteroseismic density and the density inferred from the transit light curve, the transit depth observed by the *Spitzer Space Telescope*, the RV observations of the star, and other evidence. In Section 5, we comment on possible planetary compositions. We conclude in Section 6.

2. *KEPLER* OBSERVATIONS AND ANALYSIS

Argabright et al. (2008) provided an overview of the *Kepler* instrument, and Caldwell et al. (2010) and Jenkins et al. (2010) provided a summary of its performance since launch. Borucki et al. (2011) first identified KOI 69.01 as an exoplanetary candidate (*Kepler* Input Catalog number 3544595). Our analysis of Kepler-93 is based upon 37 months of short cadence (SC) data collected in *Kepler* observing quarters Q2.3 through Q14.3, inclusive. *Kepler* SC (Gilliland et al. 2010) sampling, characterized by a 58.5 s exposure time, is crucial to the detection of the short-period asteroseismic oscillations presented by solar-type stars (see also Chaplin et al. 2011b). Kepler-93 was a subject of the asteroseismic SC survey, conducted during the first 10 months of *Kepler* operations (Chaplin et al. 2011b). They gathered one month of data per target. Only the brightest among the sub-solar mass stars possessed high enough signal-to-noise data to yield a detection in such a short time (e.g., see Chaplin et al. 2011a). With the *Kepler* instrument, they continued to gather dedicated, long-term observations of the best of these targets, Kepler-93 among them. We employed the light curves generated by the *Kepler* aperture photometry (PDC-Map) pipeline, described by Smith et al. (2012) and Stumpe et al. (2012).

2.1. Asteroseismic Estimation of Fundamental Stellar Properties

To prepare the *Kepler* photometry for asteroseismic study, we first removed planetary transits from the light curve by applying a median high-pass filter (R. Handberg et al., in preparation). We then performed the asteroseismic analysis on the Fourier power spectrum of the filtered light curve. Figure 1 shows the resulting power spectrum of Kepler-93. We find a typical spectrum of solar-like oscillations, with several overtones of acoustic (pressure, or *p*) modes of high radial order, *n*, clearly
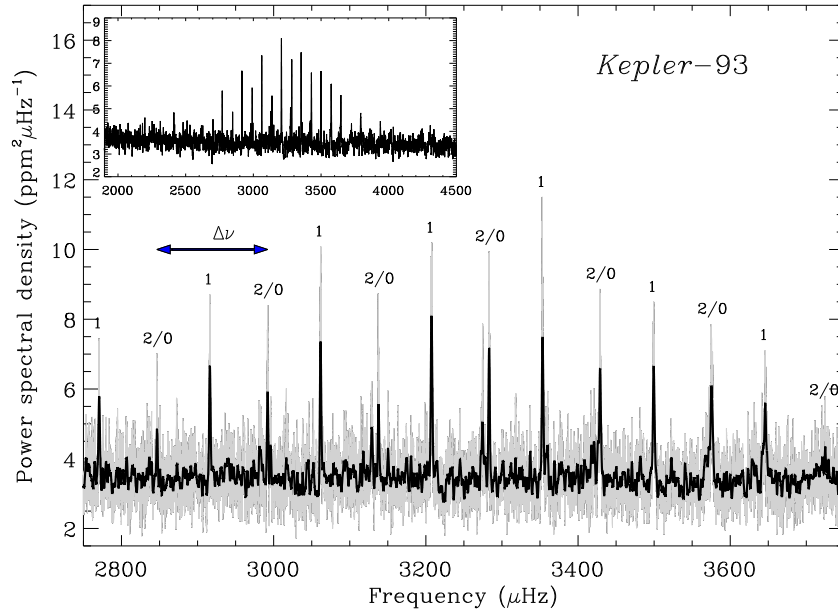
Figure 1. Power spectrum of Kepler-93. The main plot shows a close-up of the strongest oscillation modes, tagged according to their angular degree, l. The large frequency separation, here between a pair of adjacent $l = 0$ modes, is also marked. The black and gray curves show the power spectrum after smoothing with boxcars of widths 1.5 and 0.4 μHz, respectively. The inset shows the full extent of the observable oscillations.

detectable in the data. Solar-type stars oscillate in both radial and non-radial modes, with frequencies ν_{nl}, with l the angular degree. Kepler-93 shows detectable overtones of modes with $l \leqslant 2$. The dominant frequency spacing is the large separation $\Delta\nu_{nl} = \nu_{n+1\,l} - \nu_{n\,l}$ between consecutive overtones n of the same degree l.

Huber et al. (2013) reported asteroseismic properties based on the use of only average or global asteroseismic parameters. These were the average large frequency separation $\langle\Delta\nu_{nl}\rangle$ and the frequency of maximum oscillation power, ν_{max}. Here, we have performed a more detailed analysis of the asteroseismic data, using the frequencies of 30 individual p modes spanning 11 radial overtones. Using individual frequencies in the analysis enhances our ability to infer stellar properties from the seismic data. We place much more robust (and tighter) constraints on the age than is possible from using the global parameters alone.

We estimated the frequencies of the observable p modes with a "peak-bagging" Markov Chain Monte Carlo (MCMC) analysis, as per the procedures discussed in detail by (Chaplin et al. 2013; see also Carter et al. 2012). This Bayesian machinery, in addition to allowing the use of relevant priors, allows us to estimate the marginalized probability density function for each of the power spectrum model parameters. These parameters include frequencies, mode heights, mode lifetimes, rotational splitting, and inclination. This method performs well in low signal-to-noise conditions and returns reliable confidence intervals provided for the fitted parameters. We obtained a best-fitting model to the observed oscillation spectrum through optimization with an MCMC exploration of parameter space with Metropolis–Hastings sampling (e.g., see Appourchaux 2011; Handberg & Campante 2011).

We extracted estimates of the frequencies from their marginalized posterior parameter distributions. The best-fit values themselves correspond to the medians of the distributions. Table 1 lists the estimated frequencies, along with the positive and negative 68% confidence intervals. We chose not to list the estimated frequency for the $l = 2$ mode at $\simeq 3274\,\mu$Hz. This mode is possibly compromised by the presence of a prominent noise spike

Table 1
Estimated Oscillation Frequencies of Kepler-93 (in μHz)

$l = 0$	$l = 1$	$l = 2$
$2412.80 \pm 0.36/0.29$	$2481.50 \pm 0.33/0.33$	$\ldots$
$2558.14 \pm 0.84/0.96$	$2626.52 \pm 1.57/1.15$	$2692.18 \pm 0.80/0.64$
$2701.92 \pm 0.18/0.18$	$2770.62 \pm 0.23/0.25$	$2836.70 \pm 0.52/0.48$
$2846.56 \pm 0.11/0.11$	$2916.15 \pm 0.11/0.10$	$2982.49 \pm 0.25/0.27$
$2992.05 \pm 0.10/0.10$	$3061.65 \pm 0.09/0.10$	$3129.02 \pm 0.27/0.31$
$3137.70 \pm 0.14/0.12$	$3207.45 \pm 0.10/0.09$	$\ldots$
$3283.19 \pm 0.10/0.08$	$3353.39 \pm 0.10/0.10$	$3420.73 \pm 0.34/0.51$
$3428.96 \pm 0.13/0.14$	$3499.46 \pm 0.16/0.14$	$3567.75 \pm 0.65/0.70$
$3575.41 \pm 0.24/0.24$	$3645.95 \pm 0.25/0.28$	$3714.43 \pm 1.28/1.20$
$3722.32 \pm 1.24/1.08$	$3792.80 \pm 0.59/0.68$	$3860.28 \pm 1.69/1.86$
$3868.28 \pm 0.97/1.20$	$3938.88 \pm 0.89/0.73$	$\ldots$

in the power spectrum, and the posterior distribution for the estimated frequency is bimodal. The spike may be a leftover artifact of the transit, given that the frequency of the spike lies very close to a harmonic of the planetary period. We note that omitting the estimated frequency of this mode in the modeling does not alter the final solution for the star. The lowest radial orders that we detect for the $l = 0$ and $l = 1$ modes are not sufficiently prominent for $l = 2$ to yield a good constraint on the frequency. We exclude them from the table.

Figure 2 is an échelle diagram of the oscillation spectrum. We produced this figure by dividing the power spectrum into equal segments of length equal to the average large frequency separation. We arranged the segments vertically, in order of ascending frequency. The diagram shows clear ridges, comprising overtones of each degree, l. The red symbols mark the locations of the best-fitting frequencies returned by the analysis described above (with $l = 0$ modes shown as filled circles, $l = 1$ as filled triangles and $l = 2$ as filled squares).

We require a complementary spectral characterization, in tandem with asteroseismology, to determine the stellar properties of Kepler-93. From a spectrum of the star, we measure its effective temperature, T_{eff}, and its metallicity, [Fe/H]. We use these
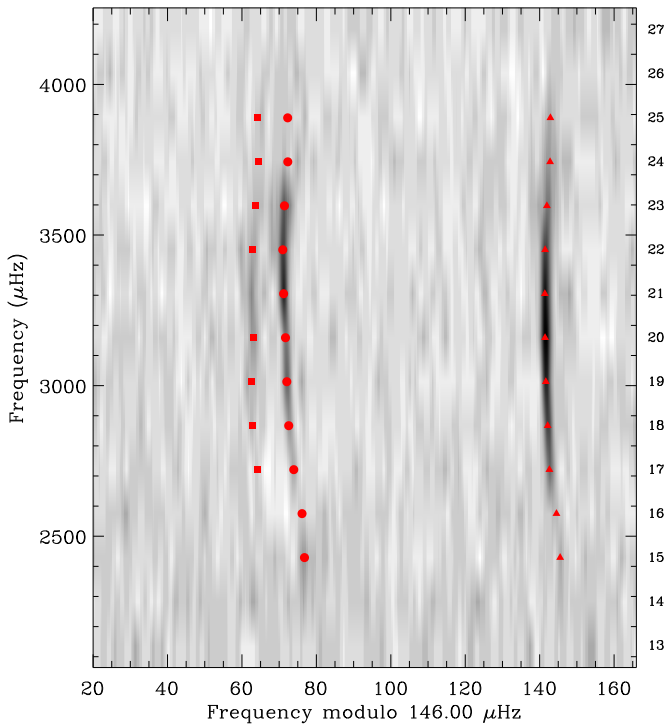
Figure 2. Échelle diagram of the oscillation spectrum of Kepler-93. The spectrum was smoothed with a 1.5 μHz Gaussian filter. The red symbols mark the best-fitting frequencies given by the peak-bagging analysis: $l = 0$ modes are shown as filled circles, $l = 1$ modes as filled triangles, and $l = 2$ modes as filled squares. The scale on the right-hand axis marks the overtone numbers n of the radial modes.

(A color version of this figure is available in the online journal.)

initial values, together with the two global asteroseismic parameters, to estimate the surface gravity, log g. Then, we repeat the spectroscopic analysis with log g fixed at the asteroseismic value, to yield the revised values of T_{eff} and [Fe/H]. We use the spectroscopic estimates of Huber et al. (2013). These values came from analysis of high-resolution optical spectra collected as part of the *Kepler* Follow-up Observing Program. To recap briefly: Huber et al. (2013), using the Stellar Parameter Classification pipeline (Buchhave et al. 2012), analyzed spectra of Kepler-93 from three sources. These were the HIRES spectrograph on the 10 m Keck telescope on Mauna Kea, the FIber-fed Echelle Spectrograph on the 2.5 m Nordic Optical Telescope on La Palma, and the Tull Coudé Spectrograph on the 2.7 m Harlan J. Smith Telescope at the McDonald Observatory. In that work, they employed an iterative procedure to refine the estimates of the spectroscopic parameters (see also Bruntt et al. 2012; Torres et al. 2012). They achieved convergence of the inferred properties (to within the estimated uncertainties) after just a single iteration.

Five members of the team (S. Basu, J.C.-D., T.S.M., V.S.A., and D.S.) independently used the individual oscillation frequencies and spectroscopic parameters to perform a detailed modeling of the host star. We adopted a methodology similar to that applied previously to the exoplanet host stars Kepler-50 and Kepler-65 (see Chaplin et al. 2013 and references therein). Full details may be found in the Appendix. The final properties presented in Table 2 are the solution set provided by J.C.-D. (whose values lay close to the median solutions). We include a contribution to the uncertainties from the scatter between all five sets of results. This was done by taking the chosen modeler's uncertainty for each property and adding (in quadrature) the stan-

dard deviation of the property from the different modeling results. Our updated properties are in good agreement with—and, as expected, more tightly constrained than—the properties in Huber et al. (2013).

We note the precision in the estimated stellar properties, in particular the age, which we estimate to slightly better than 15%. We estimate the central hydrogen abundance of Kepler-93 to be approximately 31%, which is similar to the estimated current value for the Sun. The age of Kepler-93 at central hydrogen exhaustion is predicted to be around 12.4 Gyr.

2.2. Derivation of Planetary Parameters

We estimated the uncertainty in the planetary transit parameters using the MCMC method as follows. To fit the transit light curve shape, we removed the effects of baseline drift by individually normalizing each transit. We fitted a linear function of time to the flux immediately before and after transit (specifically, from 8.6 hr to 20 minutes before first contact, equal to three transit durations, and an equivalent time after fourth contact). We employed model light curves generated with the routines in Mandel & Agol (2002), which depend upon the period P, the epoch T_c, the planet-to-star radius ratio $R_p/R_\star$, the ratio of the semi-major axis to the stellar radius $a/R_\star$, the impact parameter b, the eccentricity e, and the longitude of periastron, ω. We allowed two quadratic limb-darkening coefficients, u_1 and u_2, to vary. Our data set comprises 233 independent transits of Kepler-93b, all observed in SC mode (with exposure time 58.5 s, per Gilliland et al. 2010). We employed the Borucki et al. (2011) transit parameters from the first four months of observations as a starting point to refine the ephemeris. We allowed the time of transit to float for each individual transit signal, while fixing all other transit parameters to their published values. We then fitted a linear ephemeris to this set of transit times, and found an epoch of transit $T_0 = $ BJD 2454944.29227 ± 0.00013 and a period of 4.72673978 ± 9.7 × 10^{-7} days. We iterated this process, using the new period to fit the transit times, and found that it converged after one iteration.

We imposed an eccentricity of zero for the light curve fit, which we justify as follows. The circularization time (for modest initial e) was reported by Goldreich & Soter (1966), where a is the semimajor axis of the planet, R_p is the planetary radius, M_p is the planetary mass, $M_\star$ is the stellar mass, Q is the tidal quality factor for the planet and G is the gravitational constant:

$$t_{circ} = \frac{4}{63} \frac{1}{\sqrt{GM_\star^3}} \frac{M_p a^{13/2} Q}{R_p^5}. \qquad (1)$$

Planetary Q is highly uncertain, but we estimate a $Q = 100$ with the assumption of a terrestrial composition. This value is typical for rocky planets in our solar systems (Yoder 1995; Henning et al. 2009). We find that the circularization timescale would be 70 Myr for a 3.8 $M_\oplus$ planet orbiting a 0.91 $M_\odot$ star at 0.053 AU (we justify this mass value in Section 4.3). To achieve a circularization timescale comparable to the age of the star, Q would have to be on the order of 10^4, similar to the value of Neptune. As we discuss in Section 5.1, there is only a 3% probability that Kepler-93b has maintained an extended atmosphere. This finding renders a Neptune-like Q value correspondingly unlikely. For this reason, we assume that sufficient circularization timescales have elapsed to make the $e = 0$ assumption valid.

To fit the orbital parameters, we employed the Metropolis–Hastings MCMC algorithm with Gibbs sampling (described in

Table 2
Star and Planet Parameters for Kepler-93

Parameter	Value and 1σ Confidence Interval	
Kepler-93 (star)		
Right ascension[a]	$19^{\rm h}25^{\rm m}40\overset{\rm s}{.}39$	
Declination[a]	$+38^{\rm d}40^{\rm m}20\overset{\rm s}{.}45$	
$T_{\rm eff}$ (K)	5669 ± 75	
$R_\star$ (solar radii)	0.919 ± 0.011	
$M_\star$ (solar masses)	0.911 ± 0.033	
[Fe/H]	-0.18 ± 0.10	
$\log(g)$	4.470 ± 0.004	
Age (Gyr)	6.6 ± 0.9	
Light curve parameters	No asteroseismic prior	With asteroseismic prior
ρ (g cm^{-3})	$1.72^{+0.04}_{-0.28}$	1.652 ± 0.0060
Period (days)[b]	$4.72673978 \pm 9.7 \times 10^{-7}$	. . .
Transit epoch (BJD)[b]	$2454944.29227 \pm 0.00013$	. . .
$R_p/R_\star$	0.01474 ± 0.00017	0.014751 ± 0.000059
$a/R_\star$	$12.69^{+0.09}_{-0.76}$	12.496 ± 0.015
Inc (deg)	$89.49^{+0.51}_{-1.1}$	89.183 ± 0.044
u_1	0.442 ± 0.068	0.449 ± 0.063
u_2	0.187 ± 0.091	0.188 ± 0.089
Impact parameter	0.25 ± 0.17	0.1765 ± 0.0095
Total duration (minutes)	173.42 ± 0.36	173.39 ± 0.23
Ingress duration (minutes)	$2.52^{+0.37}_{-0.06}$	2.61 ± 0.013
Kepler-93b (planet)	No asteroseismic prior	With asteroseismic prior
R_p (Earth radii)	1.483 ± 0.025	1.478 ± 0.019
Planetary $T_{\rm eq}$ (K)	1039 ± 26	1037 ± 13
M_p (Earth masses)[c]	3.8 ± 1.5	. . .

Notes.
[a] ICRS (J2000) coordinates from the TYCHO reference catalog (Høg et al. 1998). The proper motion derived by Høg et al. (2000) -26.7 ± 1.9 in right ascension and -4.4 ± 1.8 in declination.
[b] We fit the ephemeris and period of Kepler-93 in an iterative fashion, as described in the text. We fix the other orbital parameters to fit individual transit times, and report the best linear fit to these times, rather than simultaneously fitting the transit times while imposing the asteroseismic prior.
[c] Marcy et al. (2014) describe the Kepler-93 radial velocity campaign. The stated value here is a revision, with an additional year of observations, of their published value of 2.6 ± 2.0 $M_\oplus$.

detail for astronomical use in Tegmark et al. 2004 and in Ford 2005). We first conducted this analysis using only the *Kepler* light curve to inform our fit. We incorporated the presence of correlated noise with the Carter & Winn (2009) wavelet parameterization. We fitted as free parameters the white and red contributions to the noise budget, σ_w and σ_r. The allowable range of stellar density we inferred from the light curve alone is much broader than the range of stellar densities consistent with our asteroseismic study. Crucially, they are consistent. When we fit the transit parameters independently of any knowledge of the star (allowing $a/R_\star$ to float), we found that values of $a/R_\star$ from 11.93–12.78 gave comparable fits to the light curve. This parameter varies codependently with the impact parameter (the ingress and egress times can vary within a 30 s range, from 2.5–3 minutes). We then refitted the transit light curve and apply the independent asteroseismic density constraint as follows. Rearranging Kepler's Third Law in the manner employed by Seager & Mallén-Ornelas (2003), Sozzetti et al. (2007) and Torres et al. (2008), we converted the period P (derived from photometry) and the stellar density $\rho_\star$, to a ratio of the semi-major axis to the radius of the host star, $a/R_\star$:

$$\left(\frac{a}{R_\star}\right)^3 = \frac{G P^2 (\rho_\star + p^3 \rho_p)}{3\pi}, \qquad (2)$$

where p is the ratio of the planetary radius to the stellar radius and ρ_p is the density of the planet. We will hereafter assume $p^3 \ll 1$ and consider this term negligible. We mapped the stellar density constraint, $\rho_\star = 1.652 \pm 0.006$ g cm^{-3}, to $a/R_\star = 12.496 \pm 0.015$, which we apply as a Gaussian prior in the light curve fit.

In Figure 3, we show the phased *Kepler* transit light curve for Kepler-93b, with the best-fit transit light curve overplotted. In Figure 4, we show the correlations between the posterior distributions of the subset of parameters in the model fit, as well as the histograms corresponding to each parameter. We depict two cases. In one case, we allowed the stellar density to float, in the other we applied a Gaussian prior to force its consistency with the asteroseismology analysis. We report the best-fit parameters and uncertainties in Table 2. We determined the range of acceptable solutions for each of the light curve parameters as follows. In the same manner as Torres et al. (2008), we report the most likely value from the mode of the posterior distribution, marginalizing over all other parameters. We quote the extent of the posterior distribution that encloses 68% of values closest to the mode as the uncertainty. To estimate an equilibrium temperature for the planet, we assumed that the planet possesses a Bond albedo (A_B) of 0.3 and that it radiates energy equal to the energy incident upon it. To generate physical quantities for the radius of the planet R_p, we multiplied the $R_p/R_\star$ posterior distribution by the posterior on $R_\star$. In the
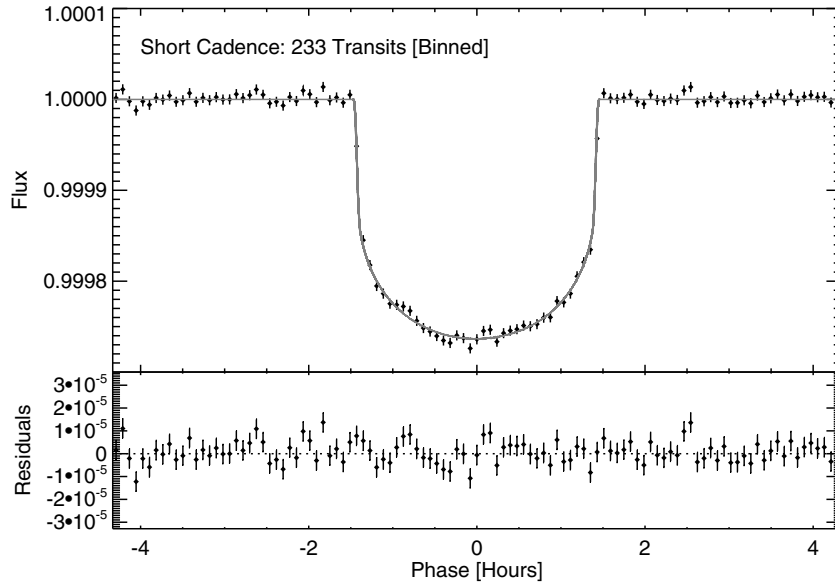
Figure 3. Kepler-93b transit light curve as a function of planetary orbital phase for quarters 1–12, gathered in short-cadence observing mode. The best-fit transit model is overplotted in gray, with residuals to the fit shown in the bottom panel.
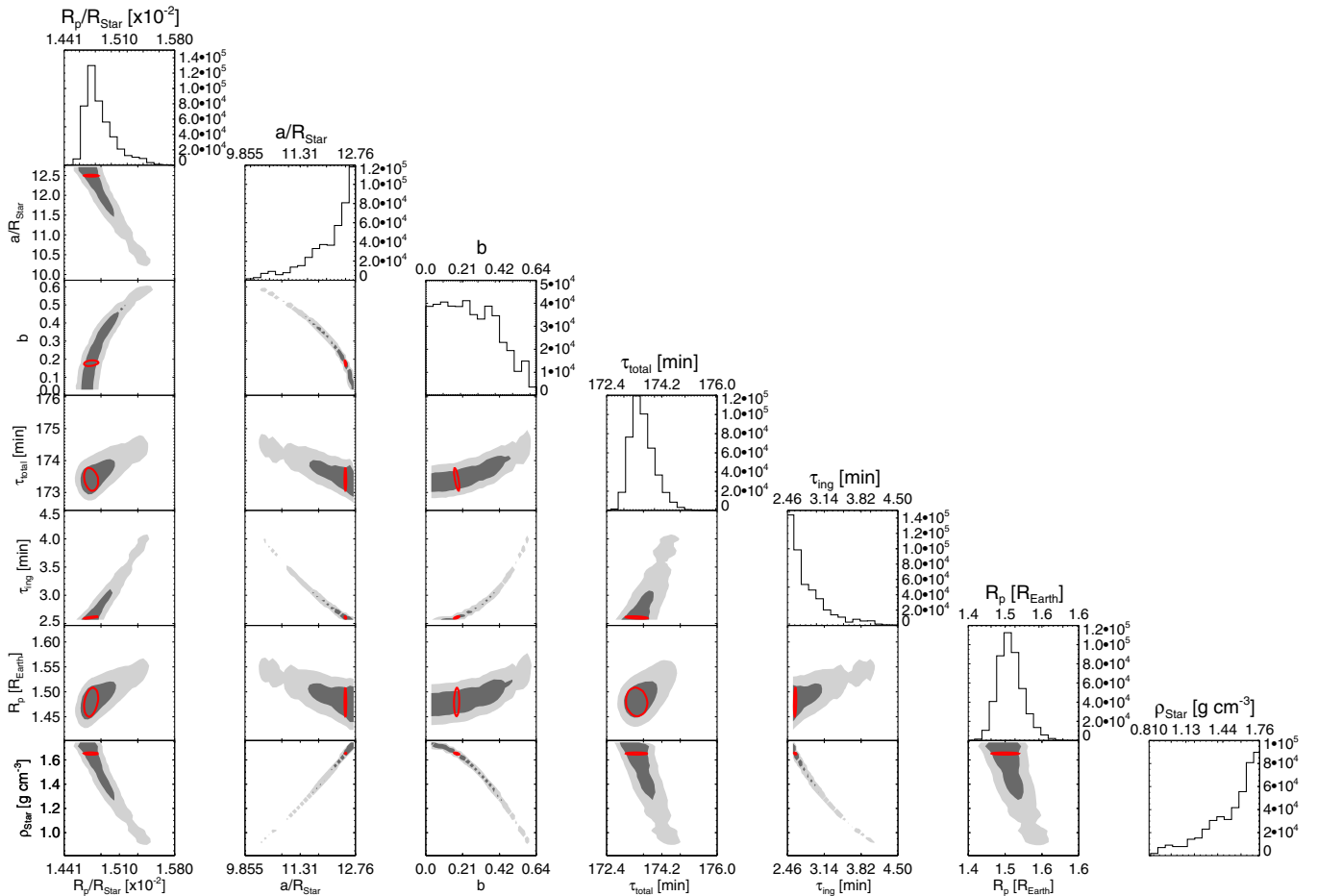

Figure 4. Markov Chain Monte Carlo probability distributions for light curve parameters of Kepler-93b. The dark gray area encloses 68% of the values in the chain, while the light gray area encloses 95% of the values. We assign the range of values corresponding to 1σ confidence from the area enclosing 68% of the values nearest to the mode of the posterior distribution for each parameter (as described in the text). When we impose the prior on $a/R_\star$ derived from asteroseismology, the 1σ confidence contours are revised to the area depicted in red.

(A color version of this figure is available in the online journal.)

Table 3
Warm *Spitzer* Observations of Kepler-93b

AOR	Date of Observation	Observing Mode	$R_p/R_\star$	$\sigma_w{}^a$ ($\times 10^{-3}$)	$\sigma_r{}^a$ ($\times 10^{-3}$)	$\alpha_{(10s)}$	$\alpha_{(Transit)}$
41009920	2010 Nov 11	No peak-up[b]	$0.008\,^{+0.012}_{-0.015}$	1.46	0.24	0.14	0.83
41010432	2010 Dec 9	No peak-up[b]	$0.002\,^{+0.013}_{-0.014}$	1.42	0.24	0.15	0.83
44381696	2011 Sep 19	No peak-up[c]	$0.0092\,^{+0.0095}_{-0.014}$	1.55	0.20	0.11	0.80
44407552	2011 Oct 7	No peak-up[c]	$0.002\,^{+0.011}_{-0.012}$	1.64	0.20	0.10	0.78
44448256	2011 Oct 26	Peak-up[c]	$0.0163\,^{+0.0046}_{-0.0080}$	1.67	0.026	0.016	0.32
44448512	2011 Oct 31	Peak-up[c]	$0.0228\,^{+0.0053}_{-0.0090}$	1.62	0.15	0.083	0.73
44448768	2011 Nov 5	Peak-up[c]	$0.0119\,^{+0.0060}_{-0.013}$	1.64	0.018	0.011	0.26

Notes.
[a] As defined in Carter & Winn (2009), for 10 s bin size.
[b] Data gathered as part of GO program 60028 (PI: Charbonneau).
[c] Data gathered as part of the IRAC Calibration program 1333 by the Spitzer Science Center.

case where we applied the asteroseismic prior, we found a planetary radius of $1.481 \pm 0.019\ R_\oplus$ with 1σ confidence. This value includes the uncertainty in stellar radius. We note that the uncertainty of $R_p/R_\star$ makes up 30% of the error budget on the planetary radius. Uncertainty on $R_\star$ itself contributes the remaining 70%. Without the asteroseismic prior on $a/R_\star$ (and the correspondingly less constrained measurement of $R_p/R_\star$), our measurement of the planetary radius is $1.485 \pm 0.27\ R_\oplus$. The contributions are nearly reversed in this case: 68% of the error in R_p is due to uncertainty in $R_p/R_\star$ and only 32% to uncertainty in the stellar radius.

The uncertainty in planetary radius of $0.019\ R_\oplus$ corresponds to 120 km. Kepler-93b is currently the planet with the most precisely measured extent outside of our solar system. A re-analysis of *Kepler*'s first rocky exoplanet Kepler-10b (Batalha et al. 2011) by Fogtmann-Schulz et al. (2014) with 29 months of *Kepler* photometry returned a similarly precise radius measurement: $1.460 \pm 0.020\ R_\oplus$. Kepler-16b (Doyle et al. 2011), with radius $8.449^{+0.028}_{-0.025}\ R_\oplus$ and Kepler-62c (Borucki et al. 2013), with radius $0.539 \pm 0.030\ R_\oplus$, are the next most precisely measured exoplanets within the published literature. The sample of these four currently comprises the only planets outside the solar system with radii measured to within $0.03\ R_\oplus$.

3. *SPITZER* OBSERVATIONS AND ANALYSIS

We gathered four transits of Kepler-93b with Warm *Spitzer* as part of program 60028 (PI: Charbonneau). These observations spanned 7.5 hr each. They are centered on the time of predicted transit, with 2 hr of out-of-transit baseline observations before ingress and after egress. The Spitzer Science Center, as part of IRAC calibration program 1333, observed Kepler-93 an additional six times to test the efficacy of the "peak-up" observational technique. This technique employs the Spitzer Pointing Control Reference Sensor, on either the science target or a nearby calibrator target, to guide the science target within 0.1 pixels of the peak sensitivity location. These observations spanned 6 hr each. They are similarly centered on transit, with out-of-transit baselines of 1.5 hr preceding and following transit. We gathered all frames at 4.5 μm. In this channel, the intrapixel sensitivity effect is lessened as compared to 3.6 μm (Ingalls et al. 2012). These observations comprise 10 total visits, of which we exclude three with the following reasoning. We do not include here the first two observations of Kepler-93 as part of program 60028 (astronomical observation requests (AORs) 39438336 and 39438592), which we gathered with exposure

time of 10 s in the full array observing mode. These frames heavily saturated due to the 10 s exposure time, and so are not useful test observations for the precision of IRAC. For all subsequent observations, we employed the 2 s exposure time and the sub-array mode, centered upon a 32×32 section of the IRAC detector. Neither do we include in our analysis the first pointing of the Spitzer Science Center to Kepler-93 (AOR 44448000). For these observations, the spacecraft pointing control relied upon gyroscopes rather than the usual star trackers. The pixel drift for these observations was unusually large, spanning several pixels, as compared to the usual 0.1 pixels. The coarse sampling of these observations does not allow meaningful removal of the pixel systematic effects. The remaining seven transits span 2010 November through 2011 November. We have listed all of the AORs associated with these transit observations of Kepler-93 in Table 3.

The limiting systematic error for time-series photometry with post-cryogenic IRAC is the variable spatial sensitivity of the pixel over the typical range of pointing drift. The undersampling of the point-spread function (PSF) results in the "pixel-phase" effect (see, e.g., Charbonneau et al. 2005; Knutson et al. 2008). The star appears brighter or dimmer as the core of the PSF lies on more or less sensitive portions of the same pixel. Typical *Spitzer* photometric observations can display variations in brightness of 8% for a star with intrinsically constant brightness (Ingalls et al. 2012). The optimal means of fitting and removing the intrapixel sensitivity variation to uncover the astrophysical signal is the subject of many papers (Charbonneau et al. 2005; Knutson et al. 2008; Ballard et al. 2010; Demory et al. 2011; Stevenson et al. 2012, among others). The traditional method for removing the pixel-phase effect is to model the variation as a polynomial in x and y. Other approaches include those of Demory et al. (2011), in which the authors included terms in their pixel model that depend upon time. Both the methods of Ballard et al. (2010) and Stevenson et al. (2012) do not rely on a particular functional form for the intrapixel sensitivity, but rather model the sensitivity behavior with a weighted sum of the brightness measurements. These weighted sums are either performed individually for each measurement (as in the Ballard et al. 2010 methodology), or interpolated onto a grid with resolution that maximizes the final precision of the light curve (as in the BLISS mapping of Stevenson et al. 2012).

We describe our particular technique for processing and extracting photometry from IRAC images in Ballard et al. (2011) and Ballard et al. (2013). We reduced all of these data in a uniform fashion, as described in these works. We deviate

here in only one way from this published process, in order to account differently for correlated noise. We include in our transit fit model the red and white noise coefficients associated with the wavelet correlated noise model developed by Carter & Winn (2009). The Transit Analysis Program (Gazak et al. 2012) incorporates this machinery, and we used it to fit our transits. This model includes the parameters σ_r and σ_w, which reflect the contributions of red (correlated) and white (Gaussian) noise budgets to the photometry. The short out-of-transit baseline associated with typical *Spitzer* transit observations makes it difficult to use the alternative residual permutation treatment (Winn et al. 2009). That method relies upon having enough observations to sample correlated noise on the timescale of the transit.

In Figure 5, we show the transit light curves and $R_p/R_\star$ posterior distributions for each transit. We also mark the spatial locations of the observations on IRAC detector. We indicate the approximate region well-mapped with a standard star by the Spitzer Science Center (Ingalls et al. 2012). Only two of the four transit observations gathered with peak-up mode fell mostly within this well-mapped region, for which there exist publicly available pixel maps (Ingalls et al. 2012). For this reason, we defaulted to the traditional self-calibration technique. For AOR 4448512, we did employ the pixel map for 4.5 μm and found similar photometric precision and the same transit depth. Therefore, we employed self-calibration uniformly for all transits. We report the measured *Spitzer* values for $R_p/R_\star$ of Kepler-93b in Table 3. We list the red and white noise coefficients, σ_r and σ_w, at the 10 s timescale for each transit. We also report the ratio between these contributing noise sources on both the 10 s and 3 hr (transit) timescales.

We note that using peak-up mode in the *Spitzer* observations of Kepler-93b improves the precision with which we measure the transit radius ratio by a factor of two. The average error bar on $R_p/R_\star$ before peak-up is 1.5×10^{-2}. After peak-up, the average error is 7.3×10^{-3}. Since the transit radius ratio itself is only 1.472×10^{-2}, we have detected the transit event in individual *Spitzer* light curves with 2σ certainty when peak-up is implemented. The improvement is reflected in the reduced values of σ_r, which encodes the presence of correlated noise in the observations: it is lower by a factor of 1.5–3. We understand the narrower posterior distributions of $R_p/R_\star$ associated with peak-up mode to be less inflated by the presence of red noise. The ratio of red/white noise for the transit duration is 0.3 with peak-up, and 0.8 without. While correlated noise is still present in the peak-up observations, it is significantly reduced.

If we combine all seven measurements of Kepler-93b gathered by *Spitzer* at 4.5 μm, then we find a planet-to-star radius ratio of $R_p/R_\star = 0.0144 \pm 0.0032$. If we consider only the values gathered with peak-up mode enabled (that is, if we use only the latter three of the seven transits) we find $R_p/R_\star$ of 0.0177 ± 0.0037, which is comparable precision with half the observing time.

4. FALSE-POSITIVE TESTS FOR KEPLER-93B

Both large-scale studies of the *Kepler* candidate sample, and individual studies of Kepler-93 specifically, consider its false positive probability. Morton & Johnson (2011) provided a priori false positive probabilities for the *Kepler* planetary candidates published by Borucki et al. (2011). They include Kepler-93 in their sample. They cite the vetting of candidates by the *Kepler* software (detailed by Batalha et al. 2010) as being already sufficient to produce a robust list of candidates. They combined

stellar population synthesis and galactic structure models to conclude a generally low false-positive rate for KOIs. Nearly all of the 1235 candidates they considered in that work have a false positive probability $<10\%$. Kepler-93, with a *Kepler* magnitude of 9.93 and a galactic latitude of $10°46$, has an a priori false positive probability of 1%. Fressin et al. (2013) considered false positive rates as a function of planetary size. The false positive rate for the radius bin relevant to Kepler-93b (1.25–2 $R_\oplus$) is $8.8 \pm 1.9\%$. Marcy et al. (2014) consider Kepler-93b specifically. They leverage the false positive machinery described by Morton (2012, which employs the transit light curve, spectroscopy, and adaptive-optics (AO) imaging) to infer a false positive probability of $<10^{-4}$. We consider the false positive probability below from the angle of stellar density, which is probed independently by asteroseismology and by the shape of the transit. We also rule out a remaining false positive possibility broached by Marcy et al. (2014), based upon the RV trend they observed.

4.1. Asteroseismic and Photometric Stellar Density Constraints

The transit light curve alone provides some constraints on the host star of the planet. False-positive scenarios in which an eclipsing binary comprising (1) two stars, or (2) a star and a planet, falls in the same aperture as the *Kepler* target star, will produce a transit signal with a diluted depth. A comparison of the detailed shape of the transit light curve to models of putative blend scenarios, as described by Torres et al. (2004), Fressin et al. (2011), and Fressin et al. (2012), constrains the parameter space in which such a blend can reside. The likelihood of such a scenario, given the additional observational constraints of spectra and AO imaging, is then weighed against the likelihood of an authentic planetary scenario. This practice returns a robust false-positive probability. Here, we rather comment on the consistency of the transit light curve with our hypothesis that it originates from a 1.48 $R_\oplus$ planet in orbit around a 0.92 $R_\odot$ star.

The *period* and *duration* of the transit will not be affected by the added light of another star. The steepness of the ingress and egress in the transit signal of Kepler-93b (enabled by the wealth of SC data on the star), which lasts between 3.0 and 2.46 minutes as we report in Table 2, reasonably precludes a non-planetary object. The transiting object passes entirely onto the disk of the star too quickly to be mimicked by an object that subtends a main sequence stellar radius. We note that a white dwarf could furnish such an ingress time, but would produce an RV variation at the 4.7 day period at the level of 100 km s^{-1}, much larger than we observe (we describe the RV observations in the following subsection). We conclude that a blend scenario (1) comprising three stars is unlikely. False positive scenario (2) involves a transiting planet system within the *Kepler* aperture that is not in orbit around the brightest star. Rather, the diluted transit depth would conspire to make the planet appear smaller than it is in reality. In this case, transit duration still constrains the density of the host star. Certain stellar hosts are immediately ruled out, because a planet orbiting them could not produce a transit as long as observed, given the eccentricity constraint implied by the short planetary period. We constrain the host from the transit light curve parameters as follows.

Winn et al. (2009) described the approximation of the transit depth for cases in which the eccentricity e is close to zero (which we assume is valid because of the short period), where $R_p \ll R_\star \ll a$ (where a is the semi-major axis of the planet's orbit) and where the impact parameter $b \ll 1 - R_p/R_\star$. In these cases, the transit timescale T, defined to be the total duration of
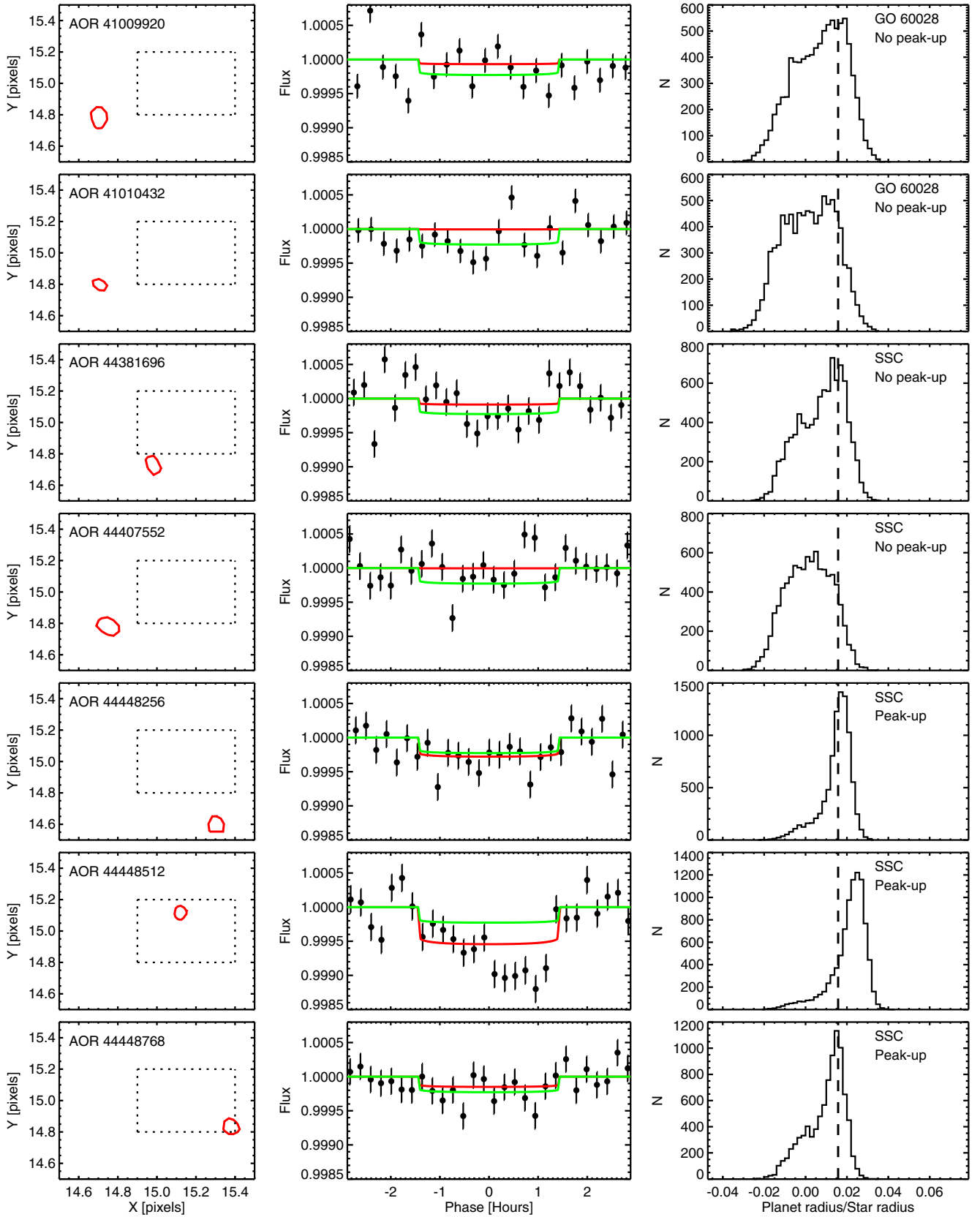
Figure 5. Left panels: location on the IRAC detector of the observations of Kepler-93. We gathered observations at the central pixel of the 32×32 subarray of IRAC. The red contour encloses 68% of centroids. We have indicated with a dotted line the approximate area which was mapped in detail with the standard star BD+67 1044 with the intent of producing a pixel flat-field (Ingalls et al. 2012). Middle panels: transits of Kepler-93b, binned to 15 minute cadence. The best-fit transit model with depth derived from the *Spitzer* observations is shown with a solid red line, while the *Kepler* transit model (with *Spitzer* 4.5 μm channel limb darkening) is shown in green. Right panels: the posterior distribution on $R_p/R_\star$ on each *Spitzer* transit. The depth measured in the *Kepler* bandpass is marked with a dashed line. The mode of pointing is noted in the upper left hand corner, as well as the program associated with the AOR.

(A color version of this figure is available in the online journal.)

the transit minus an ingress time, is related to a characteristic timescale T_0 as follows:

$$T_0 \approx \frac{T}{\sqrt{1 - b^2}}, \tag{3}$$

where

$$T_0 = \frac{R_\star P}{\pi a} \approx 13\mathrm{hr} \left(\frac{P}{1\mathrm{yr}}\right)^{1/3} \left(\frac{\rho_\star}{\rho_\odot}\right)^{-1/3}. \tag{4}$$

We computed the distribution for T_0 from our posterior distributions for the total duration, ingress duration, and impact parameter. We found that values between 170 and 184 minutes are acceptable at the 1σ confidence limit. This translates to a constraint on the exoplanet's host star density of $1.72^{+0.04}_{-0.28}$ g cm^3, as given in Table 2. The density of the *Kepler* target star measured from asteroseismology, 1.652 ± 0.006 g cm^{-3}, is within 1σ of the value inferred from the transit. This consistency lends credence to the interpretation that the bright star indeed hosts the planet.

4.2. Spitzer and Kepler Transit Depths

The transit depth we report with *Spitzer* of $R_p/R_\star = 0.0144 \pm 0.0032$ lies within 1σ of the depth measured by *Kepler* of 0.014751 ± 0.000057 (as we report in Table 2). The achromatic nature of the transit depth disfavors blended "false-positive" scenarios for Kepler-93b and render it more likely to be an authentic planet. J. M. Désert et al. (in preparation) consider the *Spitzer* transit depth, the *Spitzer* magnitude at 4.5 μm, and AO imaging to find a false-positive probability of 0.18%.

4.3. Spectra and Adaptive Optics Imaging

Marcy et al. (2014) measured the RVs of Kepler-93b. They employed Keck-HIRES spectra spanning 1132 days, from 2009 July to 2012 September. In that work, they describe their reduction and RV fitting process in detail. While they report a mass of 2.6 ± 2.0 $M_\oplus$ in that work, the addition of another 14 spectra gathered in the 2013 observing season refine this value to 3.8 ± 1.5 $M_\oplus$ (Geoffrey Marcy 2013, private communication). We employ this value, a 2.5σ detection of the mass, for the remainder of our analyses.

They report a linear RV trend in the Keck-HIRES observations of Kepler-93. This trend is present at a level of 10 m s^{-1} yr^{-1} over a baseline of three years. They conclude that the trend is caused by another object in the Kepler-93 system, and designate it Kepler-93c. They place lower limits on both its mass and period of $M > 3$ M$_{JUP}$ and $P > 5$ yr. At this lower mass limit the object would be orbiting in a near-transiting geometry (though no additional transits appear in the *Kepler* light curve). With an additional year of observations, the linear trend is still present. Because the RVs have not yet turned over, we assert that its period must in fact be larger than twice the observing baseline, which is now three years. We assume a lower limit to the period of the perturber of six years. There exists the possibility, which Marcy et al. (2014) note in their discussion of Kepler-93, that the planet is in fact orbiting the smaller body responsible for the RV drift. In this case, the planetary properties must be revisited based upon the revised stellar host. However, while the RV data alone permit this scenario, it is ruled out based upon the density inferred from the transit light curve, in tandem with other observables. We explain our reasoning here.

In Section 4.1, we argue that the host star to the planet must possess a density within the range of $1.72^{+0.04}_{-0.28}$ g cm^{-3} to be consistent with the transit duration. We compared this density to the Dartmouth stellar evolutionary models given by Dotter et al. (2008) to place an approximate constraint on the host star mass. We evaluated the Dartmouth models over a grid of metallicities (sampled at 0.1 dex from -1 to 0.5 dex) and a grid of ages between 500 Myr and 14 Gyr (sampled at 0.1 Gyr). We do not consider enhancement in alpha elements. We found that the 1σ range in observed density translates to a range of acceptable stellar masses from 0.75 to 1.23 $M_\odot$. If we assume that this putative host star is physically associated with the target star (for reasons we explore in the following paragraph), and we further require that these two stars formed within 1 Gyr of each other, then the mass is constrained to between 0.82 and 1.02 $M_\odot$. At the 3σ level of uncertainty, the density lies between 0.86 and 1.76 g cm^{-3}. The range of acceptable masses within this broader confidence interval is correspondingly 0.75–1.52 $M_\odot$. An assumption of contemporaneous formation of the two stars further constrains this range to 0.82–1.12 $M_\odot$. Therefore, we preclude stars below 0.75 $M_\odot$ as the planetary host. To be the perturber to the asteroseismic target star, the two stars are physically associated and we assume their formations to be coeval. A 0.75 $M_\odot$ star, if it possessed an age within 1 Gyr of the target star, would be between 0.7 and 1.0 mag fainter in K than the brighter target star. The exact difference in magnitude, though within this range, depends upon its exact metallicity and age. With a period greater than six years and a mass >0.75 $M_\odot$, its semimajor axis is greater than 3.9 AU.

The lack of a set of additional lines in the high-resolution spectrum brackets the upper limit on the mass and velocity of the object perturbing the bright star. Any star brighter than 0.3% the brightness of the primary star is ruled out, provided the RV difference between the bright star and the perturbing body is greater than 10 km s^{-1}. A putative star 1 mag fainter than the target star (40% its brightness) is therefore required to possess a velocity within 10 km s^{-1} of the target star. The overlap of absorption features precludes the detection of another star if their RVs are sufficiently similar. For the sake of argument, we proceed under the assumption that the additional star satisfied this condition.

Marcy et al. (2014) use Keck AO images of Kepler-93 to rule out any companion beyond $0\rlap{.}''1$ within 5 mag. We compute a physical scale corresponding to this angular size. We compare the observed *Kepler* magnitude of 9.931 to the magnitude predicted in the *Kepler* bandpass for a star with the mass, metallicity, and age of Kepler-93 (listed in Table 2) by the Dartmouth stellar evolutionary models. We find a predicted *Kepler* magnitude at a distance of 10 pc of 4.9 ± 0.1 mag. We therefore estimate that the star is approximately 100 pc away from Earth, so that $0\rlap{.}''1$ is physically equivalent to 10 AU. The minimum distance between the stars of 3.9 AU (set by the lower limit on the period of the perturber) is an angular separation of $0\rlap{.}''039$. The AO imaging rules out any object within 2 mag of the host star at this separation. The putative other host star to the planet, only 1 mag fainter, is therefore further constrained to lie in such a geometry and phase that it eluded AO detection. However unlikely, this scenario is plausible.

Therefore, we consider a hypothetical 0.75 $M_\odot$ planet-host companion to the bright star, with a semimajor axis of 3.9 AU. It possessed a velocity within 10 km s^{-1} of the host star in the high-resolution spectrum that Marcy et al. (2014) searched for a set of additional lines. At the time of the AO imaging

gathered by Marcy et al. (2014), it resided at a phase in its orbit where its projected distance from the brighter star rendered it invisible. It is then the several-year baseline of RV observations that conclusively rule out the existence of this companion. If this companion existed at 3.9 AU, the brighter star would possess an RV semi-amplitude of 15.5 km s^{-1} over the six year baseline. Given the drift in half of this period of only 45 m s^{-1}, its inclination would have to be within 0°.18 of perfectly face-on to be consistent. If it were indeed in such a face-on orientation, it would be readily detectable with AO imaging within the stated limits. We conclude, based upon the density constraint from the transit light curve in combination with published RV and spectral constraints, that the planet indeed orbits the brighter target star. Whether or not the RV trend is due to an additional Jovian planet or to a small star remains unresolved.

5. DISCUSSION

5.1. Composition of Kepler-93b

There now exist eight exoplanets with radii in the 1.0–1.5 $R_\oplus$ range with dynamically measured masses. We define the radius here as the most likely value reported by the authors, and define a mass detection as residing more than two standard deviations from a mass of zero. From smallest to largest, these are Kepler-102d (Marcy et al. 2014), Kepler-78b (Howard et al. 2013; Pepe et al. 2013), Kepler-100b (Marcy et al. 2014), Kepler-10b (Batalha et al. 2011), Kepler-406b (Marcy et al. 2014), Kepler-99b (Marcy et al. 2014), Kepler-93b, and Kepler-36b (Carter et al. 2012). The mass of Kepler-93b is detected by Marcy et al. (2014) at $3.8 \pm 1.5\ M_\oplus$. This translates to a density of 6.3 ± 2.6 g cm^{-3}. Among the worlds smaller than 1.5 $R_\oplus$, the density of Kepler-93b is statistically indistinguishable from those of Kepler-78b, Kepler-36b, and Kepler-10b.

In Figure 6, we show the mass and radius measurements of the current sample of exoplanets smaller than 2.2 $R_\oplus$. The figure does not include the growing population of exoplanets with upper mass limits from RV measurements or dynamical stability arguments. We consider whether there exists evidence for a trend of bulk density with equilibrium temperature for this subset of planets. Their densities range from 1.3 g cm^{-3} for KOI 314.02 (Kipping et al. 2014), to 18 g cm^{-3} for Kepler-100b (Marcy et al. 2014). The exact cutoff of the transition between rocky and gaseous worlds likely resides between 1.5 and 2 $R_\oplus$, with both observations and theory informing our understanding (Marcy et al. 2014 and Mordasini et al. 2012, respectively, among others). Rogers (2014) determined that the value at which half of planets are rocky and half gaseous occurs no higher than 1.9 $R_\oplus$. Whether or not equilibrium temperature also affects this relationship is what we test here. Carter et al. (2012) studied the same parameter space for the known exoplanets with $M < 10\ M_\oplus$. They noted a dearth of gaseous planets (densities less than 3.5 g cm^{-3}) hotter than 1250 K. They posited that evaporation plays a role in stripping the atmospheres from the planets with higher insolation. In Figure 7, we overplot in gray the region where Carter et al. (2012) observed a lack of planets. We note first that the temperatures of exoplanets have large uncertainties. This is true even for worlds such as Kepler-78b, for which Sanchis-Ojeda et al. (2013) robustly detected the light emanating from the planet alone. For the purposes of this investigation, we assign the temperature reported by the authors in their discovery papers. We use the mean value within the range of possible temperatures, if the authors quote their uncertainty. If temperature was not among the quoted pa-
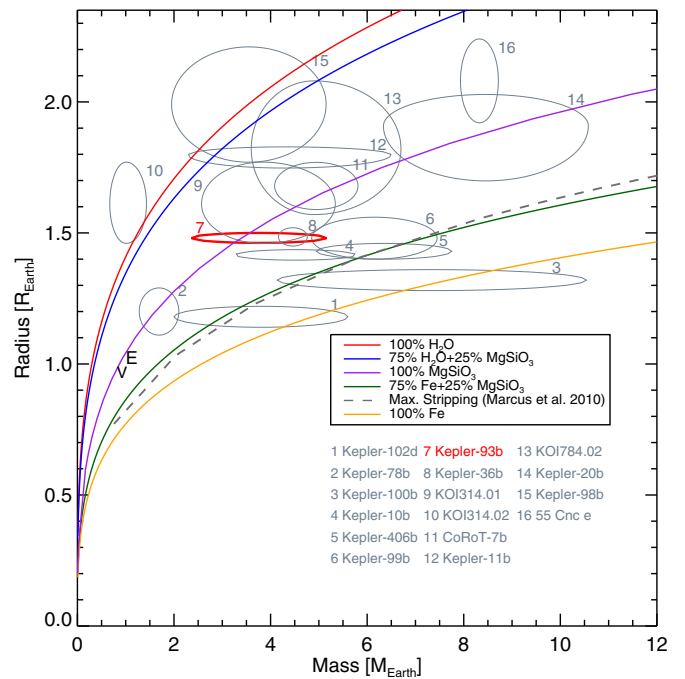

Figure 6. Masses and radii for all known planets with radii $<2\ R_\oplus$ (within 1σ uncertainty). We have included only planets with detected mass measurements of at least 2σ certainty. We overplotted the theoretical mass–radius curves from Zeng & Sasselov (2013) for five cases (in order of increasing density): pure water, a mixture of 75% water and 25% magnesium silicate, pure magnesium silicate, a mixture of 75% iron and 75% magnesium silicate, and 100% iron. We also include the theoretical maximum collisional stripping limit from Marcus et al. (2010), below which planets should not be able to acquire a larger iron fraction.

(A color version of this figure is available in the online journal.)

rameters, we use the equilibrium temperature value from the NASA Exoplanet Archive.[18] We assign the range in density uncertainty from the quoted mass and radius uncertainties. As we indicate in Figure 7, we find a flat relationship between equilibrium temperature and density, indicating that temperature is not meaningfully predictive of the densities of planets within this radius range. However, this calculation presupposes no theoretical upper limit to density. Kepler-100b, for example, must constitute 70%–100% iron by mass to be consistent with its measured properties. Marcus et al. (2010) derived an upper limit to iron mass fraction, assuming a collisional stripping history for denser worlds. This framework cannot lead to rocky planets with a fractional iron content above 75% (this fraction varies slightly with radius). We apply the hard prior that each planet cannot possess a density greater than the value computed by Marcus et al. (2010) for this mass, and recompute the best-fit line. Now, we find that the best-fit line is one that predicts increasing density with stronger insolation, but the detection is indistinguishable from a flat line. The prior does meaningfully change the mean density of worlds between 1.0 and 1.5 $R_\oplus$. Taking their reported mass and radius measurements, the mean density of planets with $1.0 < R_\oplus < 1.5$ is 10.0 ± 1.5 g cm^{-3}, nearly twice as dense as Earth. This range is barely theoretical supportable, since worlds between 1.0 and 1.5 $R_\oplus$ have maximum theoretically plausible densities of 11 g cm^{-3}. We would conclude that Kepler-93b, with density of 6.3 ± 2.6 g cm^{-3}, lies within the lightest 9% of planets within $1.0 < R_\oplus < 1.5$. Earth, with a density of 5.5 g cm^{-3}, resides 3σ from the mean

---

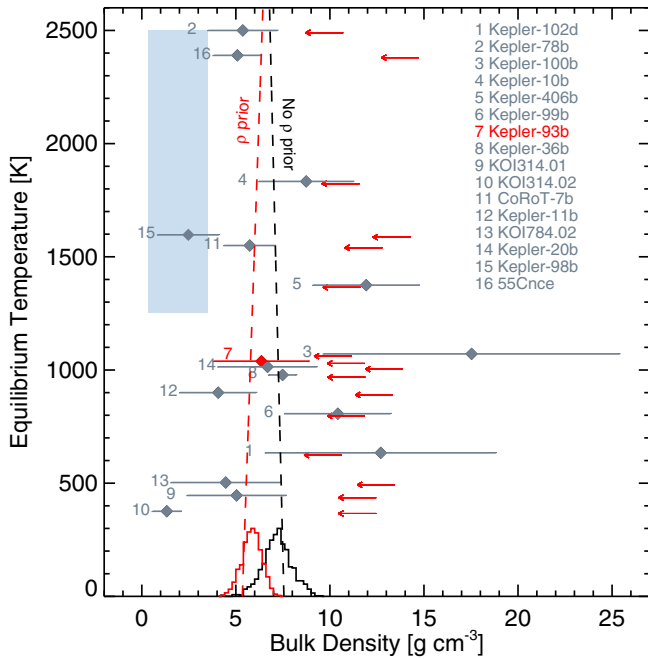[18] http://exoplanetarchive.ipac.caltech.edu/

Figure 7. Planetary bulk density as a function of equilibrium temperature, for known exoplanets smaller than 2.2 $R_\oplus$. Individual planets are labeled in order of their radius, from smallest to largest. These labels are the same as in Figure 6. Red arrows immediately to the right of each error bar mark the upper limit on density from Marcus et al. (2010). Densities heavier than this value are not theoretically supportable, given the collisional-stripping model. Two dashed lines depict the best-fit relation between equilibrium temperature and density. The black line allows for unphysical densities, while the red line does not. The posterior distribution on the "mean" density of the sample is indicated on the bottom axis, for the same two cases. The shaded region corresponds to the parameter space in which Carter et al. (2012) observed a dearth of planets.

(A color version of this figure is available in the online journal.)
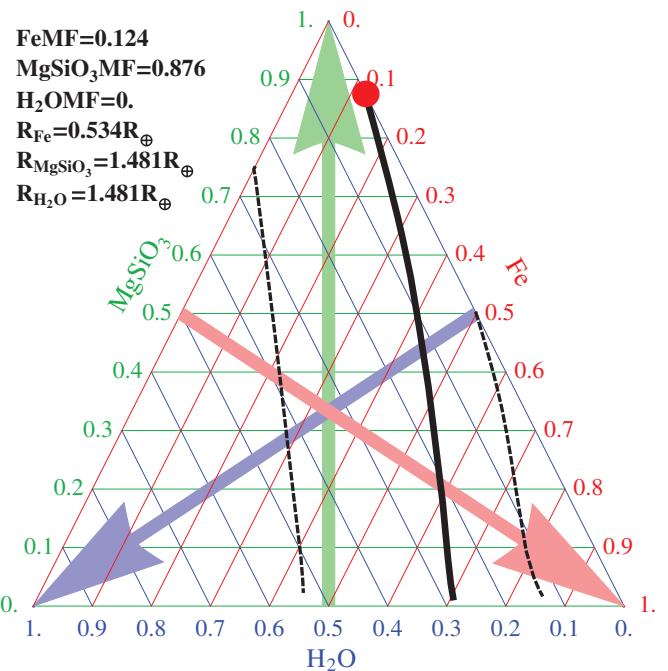

Figure 8. Ternary diagram for Kepler-93b, using the models of Zeng & Sasselov (2013) comprised of water, magnesium silicate, and iron. The compositional degeneracy for the best-fit value of mass and radius is depicted with a solid line, while the allowable range for compositions within the radius and mass uncertainty is indicated with dotted lines. The model with no water is indicated with a red circle. The mass fraction and radial extent of each element (assuming complete differentiation) associated with this composition are indicated in upper left.

(A color version of this figure is available in the online journal.)

density of similarly sized worlds and ought to be rare indeed. In contrast, applying a prior of plausible density returns a mean value of 7.3 ± 0.9 g cm^{-3}, and we would conclude that both Earth and Kepler-93b possess average density among similarly sized worlds.

We compare the mass and radius of Kepler-93b against the theoretical compositions computed by Zeng & Sasselov (2013) for differing budgets of water, magnesium silicate, and iron. Figure 8 depicts the compositional ternary diagram for Kepler-93b, employing the theoretical models of Zeng & Sasselov (2013). A 100% magnesium silicate planet at the radius of Kepler-93b would have a mass of 3.3 $M_\oplus$, which is only 0.3σ removed from the measured mass of 3.8 ± 1.5 $M_\oplus$. All mass fractions of magnesium silicate are plausible within the 1σ error bar, though a pure water and iron planet is barely theoretically supportable. Within the 1σ range in radius and mass that we report, iron mass fractions above 70% are unphysical (Marcus et al. 2010), and the entire remaining composition would need to be water for the planet to contain no rock. Given the age of the star of 6.6 ± 0.9 Gyr, we consider it possible that all water content has been lost within Kepler-93b through outgassing. If this were the case, the planet would comprise 12.5% iron by mass, and 87.5% magnesium silicate.

5.2. Likelihood of Extended Atmosphere

To estimate of the likelihood of Kepler-93b's possessing an extended atmosphere, we first examine the criterion for Jean's escape for diatomic hydrogen. Given the temperature of 1037 ± 13 K that we infer based upon the planet's insolation (and an as-

sumption for its albedo of 0.3), the root-mean-squared velocity within the Maxwell–Boltzmann distribution for an H_2 molecule is 3600 m s^{-1}. In contrast, the escape speed from Kepler-93b is 18 000 m s^{-1}. We assume that species with root-mean-square speeds higher than one-sixth the escape speed will be lost from the atmosphere Seager (2010), but we find $v_{\rm rms/v_{esc}} \approx 5$ for diatomic hydrogen, and so atmospheres of all kinds are theoretically plausible. We employ the metric created by Kipping et al. (2013) to assign a probability to the likelihood of an extended atmosphere, given the measured mass and radius posterior distributions. They provide a framework to calculate the posterior on the quantity $R_{\rm MAH}$, the physical extent of the planet's atmosphere atop a minimally dense core of water as derived by Zeng & Sasselov (2013). They assume that the bulk composition of a super-Earth-sized planet cannot be made of a material lighter than water, and so if the radius of the planet is significantly larger than inferred from this lower physical limit on the density, it must possess an atmosphere to match the observed radius. We apply the radius for Kepler-93b from Table 2 of $1.478^{+0.019}_{-0.019}$ $R_\oplus$ and the mass of 3.8 ± 1.5 $M_\oplus$ to find a probably of 3% that the planet possesses an extended atmosphere. Kepler-93b is therefore 97% likely to be rocky in composition. In comparison, the published radius and mass posterior distributions for Kepler-36c and Kepler-10b return a probability for an extended atmosphere of <0.01% and 0.2%, respectively. These smaller probabilities, even though Kepler-36c and Kepler-10b are nearly the same size as Kepler-93b, are attributable to the slightly higher mass estimates for the former two worlds. We conclude that there exists a small but non-zero probability that the planet possesses a significantly larger atmosphere than the two planets most similar to it.
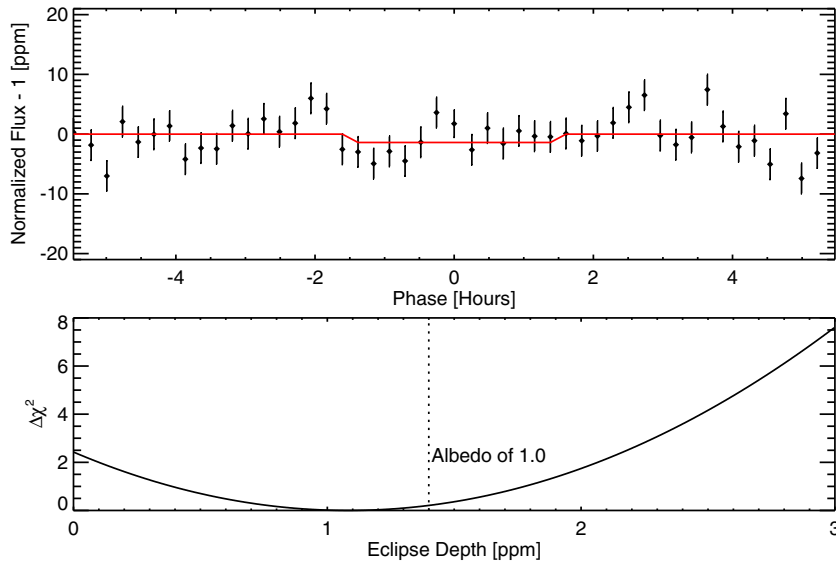
Figure 9. Top panel: light curve of Kepler-93b, centered on an orbital phase of 0.5. We have overplotted the eclipse model corresponding to the maximum albedo of 1.0. Bottom panel: the χ^2 improvement afforded by eclipse models, as a function of the depth of the secondary eclipse. We find only an upper limit to the eclipse depth: it must be <2.5 ppm at a phase of 0.5, with 2σ confidence. This is not physically constraining, since the predicted depth produced by a planet with albedo of 1.0 is 1.4 ppm.

(A color version of this figure is available in the online journal.)

5.3. Secondary Eclipse Constraint

Assuming again the Bond albedo (A_B) of 0.3, the expected relative depth due to reflected light is given by $\delta_{\rm ref} = A_B(R_p/a)^2$. This value is 0.4 ppm for $A = 0.3$, but could be as high as 1.4 ppm for an albedo of 1.0. The expected secondary eclipse depth due to the emitted light of the planet is given by $\delta_{\rm em} = (R_p/R_\star)^2 B_\lambda(T_p)/B_\lambda(T_\star)$. Assuming again an albedo of 0.3, wavelength of 700 nm (in the middle of the *Kepler* bandpass) to estimate $B_\lambda(T)$, $\delta_{\rm em}$ is of order 10^{-10} and so contributes negligibly to the expected eclipse depth. In Figure 9, we show the phased light curve, binned in increments of 12 minutes, and centered on a phase of 0.5. We have treated these data similarly to the data in-transit, by fitting a linear baseline with time to the observations immediately adjacent to each predicted eclipse and dividing this line from the eclipse observations. The scatter per 15 minute error bar is 2.4 ppm, so for a 173 minute secondary eclipse, the predicted depth error bar at 1σ is 0.7 ppm. All physical depths (that is, <1.4 ppm) should therefore furnish χ^2 fits within 2σ of one another. We conclude that the data cannot meaningfully distinguish between eclipse depths within the physical range of albedos. Only eclipses deeper than 6 ppm are ruled out at 3σ significance, and this value is too high to be physically meaningful. We repeated the eclipse search in intervals of 1 hr from phases of 0.4–0.6 of the orbital phase (corresponding to 11 hr preceding and following the eclipse time at 0.5 the orbital phase). We produce a new eclipse light curve to test each putative eclipse time, by fitting the baseline to out-of-eclipse observations adjacent to the new ephemeris (to avoid normalizing out any authentic eclipse signal). We report no statistically significant detection of an eclipse signal over this range, and set an upper limit on the eclipse depth of 2.5 ppm with 2σ confidence.

6. CONCLUSIONS

We have presented the characterization of Kepler-93b, a rocky planet orbiting one of the brightest stars studied by *Kepler*.

1. We measure the asteroseismic spectrum of Kepler-93. With a mass of $0.911 \pm 0.033\,M_\odot$, it is one of the lowest mass subjects of asteroseismic study. We measure its radius to be $0.919 \pm 0.011\,R_\odot$ and its mean density to be 1.652 ± 0.006 g cm^{-3}.

2. We measure the radius of Kepler-93b to be $1.481 \pm 0.019\,R_\oplus$. Kepler-93b is the most precisely measured planet outside of the solar system, and among the only four exoplanets whose sizes are known to within 0.03 $R_\oplus$. Applying our knowledge of the star from asteroseismology to fit the transit light curve reduced the uncertainty on the planet radius by a third.

3. We measure a consistent transit depth for Kepler-93b with both *Kepler* and *Spitzer* observations. We used Kepler-93b as a test subject for the peak-up observing mode with *Spitzer*. We find that peak-up reduces the uncertainty with which we measure the planet-to-star radius ratio by a factor of two.

4. From the RV measurements of the mass of Kepler-93b, we conclude that it possesses a mean density of 6.3 ± 2.6 g cm^{-3}. It likely has a terrestrial composition. Applying a theoretical density prior on the known exoplanets smaller than 1.5 $R_\oplus$, we find that the average density of planets in this range is 7.3 ± 0.9 g cm^{-3} (this density is nearly unphysically high without the prior). We conclude that Kepler-93b has a density that is average among similarly sized planets.

The best way for increasing our knowledge about the planet's nature is by continued RV observations of the star. Firstly, an extended baseline of RV measurements will constrain the nature of Kepler-93c, the long-period companion. The current four year baseline only proves that this object has an orbital period longer than six years, and that it must be larger than three Jupiter masses. The story of the formation of Kepler-93b and its migration to its current highly irradiated location will be illuminated in part by an understanding of this companion's mass and eccentricity. Secondly, the continued monitoring of

the shorter-term RV signature of Kepler-93b will allow us to winnow down the allowable parameter space of its composition. We conduct a sample calculation of the likelihood of an extended atmosphere on Kepler-93b with a refined mass estimate of the planet. If the uncertainty was reduced by a factor of two from its current value of 1.5–$M_\oplus$, and the most probable value were refined to 1.5σ below the current most probable value of 3.8 $M_\oplus$, then the likelihood of an extended atmosphere is upwardly revised to 25%. The asteroseismic study of this world has returned a strong constraint of 6.6 ± 0.9 Gyr on the planet's age. If it is plausible for the water on the planet to be outgassed and lost under its insolation conditions on this timescale, we could reconsider the magnesium and iron content of its core. If the planet is made of only the latter two materials, models indicate that its iron mass fraction would be only 40% that of the Earth's, which is 32.5% iron by mass (Morgan & Anders 1980). The unprecedented determination of the radius of Kepler-93b to 120 km speaks to the increasing precision with which we are able to examine planets orbiting other stars. Exoplanetary systems such as Kepler-93 that can support simultaneous studies of stellar structure, exoplanetary radius, and exoplanetary mass comprise valuable laboratories for future study.

APPENDIX

ESTIMATION OF STELLAR PROPERTIES USING OSCILLATION FREQUENCIES

Five members of the team (S.B., J.C.-D., T.S.M., V.S.A., and D.S.) performed a detailed modeling of the host star using estimates of the individual oscillation frequencies and spectroscopic parameters as input. The estimated properties from the global asteroseismic parameters analysis presented in Huber et al. (2013) were used either as starting guesses or as a guideline check for initial results.

S.B. and J.C.-D. adopted the same analysis procedures discussed in detail in Chaplin et al. (2013), using, respectively, models from the Yale stellar evolution code, YREC (Demarque et al. 2008) and the ASTEC code (Christensen-Dalsgaard 2008b; for J.C.-D.'s analysis; see also Silva Aguirre et al. 2013). T.S.M. used the Asteroseismic Modeling Portal (Metcalfe et al. 2009; Woitaszek et al. 2009), a web-based tool linked to TeraGrid computing resources that runs an automated search based on a parallel genetic algorithm. Further details on the application to asteroseismic data may again be found in Chaplin et al. (2013). Here, in addition to the individual oscillation frequencies, two sets of frequency ratios—$r_{02}(n)$ and $r_{010}(n)$ (Roxburgh & Vorontsov 2003)—were also used as seismic inputs (see also Metcalfe et al. 2014 for further information).

V.S.A. computed models using the Garching Stellar Evolution Code (GARSTEC; Weiss & Schlattl 2008). The input physics included the OPAL equation of state (Rogers & Nayfonov 2002), OPAL opacities at high temperatures (Iglesias & Rogers 1996) and Ferguson et al. (2005) opacities at low temperatures. The nuclear reaction rates were those of the NACRE compilation (Angulo et al. 1999), including the updated cross section for $^{14}N(p, \gamma)^{15}O$ from Formicola et al. (2004). Convective regions were treated under the mixing-length formalism of Kippenhahn et al. (2013), while diffusion of helium and heavy elements was included following the prescription of Thoul et al. (1994).

A grid of stellar models was constructed spanning a mass range of 0.8–1.0 $M_\odot$, with a varying initial helium abundance between 0.22 and 0.30. Five different compositions were determined for each helium value, which covered the 1σ range in metallicity determined from the spectroscopy, at the observed average large frequency separation. The best-matching model was determined from a fit to the spectroscopic data and the frequency separation ratios r_{010} and r_{02} (e.g., Roxburgh & Vorontsov 2003; Silva Aguirre et al. 2011). Final properties and uncertainties were determined from weighted means and standard deviations of properties of all models in the selected grid, with weights fixed by the χ^2 of the separation ratios and spectroscopic values (with allowance made for the correlations between the separation ratios; see Silva Aguirre et al. 2013 for a detailed description).

D.S. made use of the MESA stellar evolution code (Paxton et al. 2011). The "astero" mode of MESA has several ways of matching stellar models to observational data, including data from spectroscopy and asteroseismology (Paxton et al. 2013). The method used in this work employs an automated simplex search algorithm to optimize the model parameters that best reproduce the observations. Each model evaluation was initiated in the fully convective, pre-main-sequence stage, and evolved until the χ^2 between the model parameters and observational parameters had become significantly larger than its minimum value along that particular evolutionary track. Repeated tracks with different initial values for mass, helium content, [Fe/H], and mixing length parameter were controlled by the simplex algorithm, based on the minimum χ^2 of previous tracks. The χ^2 comprised contributions from the asteroseismic data (frequencies and the frequency ratios, r_{02} and r_{010}) and from spectroscopy (T_{eff}, [Fe/H]). Model frequencies were calculated by ADIPLS (Christensen-Dalsgaard 2008a) from an internal call within MESA, and were corrected for near-surface effects according to the prescription by Kjeldsen et al. (2008). The uncertainties of the best-fitting model properties were found by evaluating locations on the χ^2 surface where $\min(\chi^2 + 1)$ was reached.

We used the OPAL equation of state (Rogers & Nayfonov 2002), the OPAL opacities (Iglesias & Rogers 1996), with low-temperature opacities from Ferguson et al. (2005). Nuclear reaction rates were from NACRE (Angulo et al. 1999), with updates for $^{14}\mathrm{N}(p, \gamma)^{15}\mathrm{O}$ (Imbriani et al. 2004, 2005) and $^{12}\mathrm{C}(\alpha, \gamma)^{16}\mathrm{O}$ (Kunz et al. 2002). Models used a fixed value for exponential overshoot ($f_{\mathrm{ov}} = 0.015$, roughly equivalent to a linear (fully mixed) overshoot of 0.15 times the pressure scale height). Diffusion was not turned on. Convection was treated according to mixing-length theory. We refer the reader to Paxton et al. (2011) for further details.

REFERENCES

Angulo, C., Arnould, M., Rayet, M., et al. 1999, NuPhA, 656, 3
Appourchaux, T. 2011, in Asteroseismology, ed. P. Pallé (Canary Islands Winter School of Astrophysics, Vol. 23; Cambridge: Cambridge Univ. Press), 22
Argabright, V. S., VanCleve, J. E., Bachtell, E. E., et al. 2008, Proc. SPIE, 7010, 70102L-1
Ballard, S., Charbonneau, D., Deming, D., et al. 2010, PASP, 122, 1341
Ballard, S., Charbonneau, D., Fressin, F., et al. 2013, ApJ, 773, 98
Ballard, S., Fabrycky, D., Fressin, F., et al. 2011, ApJ, 743, 200
Barclay, T., Rowe, J. F., Lissauer, J. J., et al. 2013, Natur, 494, 452
Batalha, N. M., Borucki, W. J., Bryson, S. T., et al. 2011, ApJ, 729, 27
Batalha, N. M., Borucki, W. J., Koch, D. G., et al. 2010, ApJL, 713, L109
Borucki, W. J., Agol, E., Fressin, F., et al. 2013, Sci, 340, 587
Borucki, W. J., Koch, D. G., Basri, G., et al. 2011, ApJ, 736, 19
Borucki, W. J., Koch, D. G., Batalha, N., et al. 2012, ApJ, 745, 120
Brown, T. M., & Gilliland, R. L. 1994, ARA&A, 32, 37
Bruntt, H., Basu, S., Smalley, B., et al. 2012, MNRAS, 423, 122
Buchhave, L. A., Latham, D. W., Carter, J. A., et al. 2011, ApJS, 197, 3
Buchhave, L. A., Latham, D. W., Johansen, A., et al. 2012, Natur, 486, 375
Caldwell, D. A., van Cleve, J. E., Jenkins, J. M., et al. 2010, Proc. SPIE, 7731, 773117-1
Carter, J. A., Agol, E., Chaplin, W. J., et al. 2012, Sci, 337, 556
Carter, J. A., & Winn, J. N. 2009, ApJ, 704, 51
Chaplin, W. J., Kjeldsen, H., Bedding, T. R., et al. 2011a, ApJ, 732, 54
Chaplin, W. J., Kjeldsen, H., Christensen-Dalsgaard, J., et al. 2011b, Sci, 332, 213
Chaplin, W. J., Sanchis-Ojeda, R., Campante, T. L., et al. 2013, ApJ, 766, 101
Charbonneau, D., Allen, L. E., Megeath, S. T., et al. 2005, ApJ, 626, 523
Christensen-Dalsgaard, J. 2008a, Ap&SS, 316, 113
Christensen-Dalsgaard, J. 2008b, Ap&SS, 316, 13
Cochran, W. D., Fabrycky, D. C., Torres, G., et al. 2011, ApJS, 197, 7
Demarque, P., Guenther, D. B., Li, L. H., Mazumdar, A., & Straka, C. W. 2008, Ap&SS, 316, 31

Demory, B.-O., Gillon, M., Deming, D., et al. 2011, A&A, 533, A114
Désert, J.-M., Bean, J., Miller-Ricci Kempton, E., et al. 2011, ApJL, 731, L40
Dotter, A., Chaboyer, B., Jevremović, D., et al. 2008, ApJS, 178, 89
Doyle, L. R., Carter, J. A., Fabrycky, D. C., et al. 2011, Sci, 333, 1602
Dressing, C. D., & Charbonneau, D. 2013, ApJ, 767, 95
Fazio, G. G., Hora, J. L., Allen, L. E., et al. 2004, ApJS, 154, 10
Ferguson, J. W., Alexander, D. R., Allard, F., et al. 2005, ApJ, 623, 585
Fogtmann-Schulz, A., Hinrup, B., Van Eylen, V., et al. 2014, ApJ, 781, 67
Ford, E. B. 2005, AJ, 129, 1706
Formicola, A., Imbriani, G., Costantini, H., et al. 2004, PhLB, 591, 61
Fressin, F., Torres, G., Charbonneau, D., et al. 2013, ApJ, 766, 81
Fressin, F., Torres, G., Désert, J.-M., et al. 2011, ApJS, 197, 5
Fressin, F., Torres, G., Rowe, J. F., et al. 2012, Natur, 482, 195
Gautier, T. N., III, Charbonneau, D., Rowe, J. F., et al. 2012, ApJ, 749, 15
Gazak, J. Z., Johnson, J. A., Tonry, J., et al. 2012, AdAst, 2012, 697967
Gilliland, R. L., Jenkins, J. M., Borucki, W. J., et al. 2010, ApJL, 713, L160
Gilliland, R. L., Marcy, G. W., Rowe, J. F., et al. 2013, ApJ, 766, 40
Gilliland, R. L., McCullough, P. R., Nelan, E. P., et al. 2011, ApJ, 726, 2
Goldreich, P., & Soter, S. 1966, Icar, 5, 375
Grillmair, C. J., Carey, S. J., Stauffer, J. R., et al. 2012, Proc. SPIE, 8448, 84481I-1
Handberg, R., & Campante, T. L. 2011, A&A, 527, A56
Henning, W. G., O'Connell, R. J., & Sasselov, D. D. 2009, ApJ, 707, 1000
Høg, E., Fabricius, C., Makarov, V. V., et al. 2000, A&A, 355, L27
Høg, E., Kuzmin, A., Bastian, U., et al. 1998, A&A, 335, L65
Howard, A. W., Sanchis-Ojeda, R., Marcy, G. W., et al. 2013, Natur, 503, 381
Howell, S. B., Rowe, J. F., Bryson, S. T., et al. 2012, ApJ, 746, 123
Huber, D., Chaplin, W. J., Christensen-Dalsgaard, J., et al. 2013, ApJ, 767, 127
Iglesias, C. A., & Rogers, F. J. 1996, ApJ, 464, 943
Imbriani, G., Costantini, H., Formicola, A., et al. 2004, A&A, 420, 625
Imbriani, G., Costantini, H., Formicola, A., et al. 2005, EPJA, 25, 455
Ingalls, J. G., Krick, J. E., Carey, S. J., et al. 2012, Proc. SPIE, 8442, 844214-1
Jenkins, J. M., Caldwell, D. A., Chandrasekaran, H., et al. 2010, ApJL, 713, L120
Kippenhahn, R., Weigert, A., & Weiss, A. 2013, Stellar Structure and Evolution (Berlin: Springer)
Kipping, D. M., Nesvorný, D., Buchhave, L. A., et al. 2014, ApJ, 784, 28
Kipping, D. M., Spiegel, D. S., & Sasselov, D. D. 2013, MNRAS, 434, 1883
Kjeldsen, H., Bedding, T. R., & Christensen-Dalsgaard, J. 2008, ApJL, 683, L175
Knutson, H. A., Charbonneau, D., Allen, L. E., Burrows, A., & Megeath, S. T. 2008, ApJ, 673, 526
Knutson, H. A., Charbonneau, D., Allen, L. E., et al. 2007, Natur, 447, 183
Kunz, R., Fey, M., Jaeger, M., et al. 2002, ApJ, 567, 643
Lissauer, J. J., Marcy, G. W., Bryson, S. T., et al. 2014, ApJ, 784, 44
Mandel, K., & Agol, E. 2002, ApJL, 580, L171
Marcus, R. A., Sasselov, D., Hernquist, L., & Stewart, S. 2010, ApJL, 712, L73
Marcy, G. W., Isaacson, H., Howard, A. W., et al. 2014, ApJS, 210, 20
Metcalfe, T. S., Creevey, O. L., & Christensen-Dalsgaard, J. 2009, ApJ, 699, 373
Metcalfe, T. S., Creevey, O. L., Dogan, G., et al. 2014, ApJ, submitted (arXiv:1402.3614)
Mordasini, C., Alibert, Y., Georgy, C., et al. 2012, A&A, 547, A112
Morgan, J. W., & Anders, E. 1980, PNAS, 77, 6973
Morton, T. D. 2012, ApJ, 761, 6
Morton, T. D., & Johnson, J. A. 2011, ApJ, 738, 170
Nutzman, P., Gilliland, R. L., McCullough, P. R., et al. 2011, ApJ, 726, 3
Paxton, B., Bildsten, L., Dotter, A., et al. 2011, ApJS, 192, 3
Paxton, B., Cantiello, M., Arras, P., et al. 2013, ApJS, 208, 42
Pepe, F., Cameron, A. C., Latham, D. W., et al. 2013, Natur, 503, 377
Petigura, E. A., Howard, A. W., & Marcy, G. W. 2013a, PNAS, 110, 19273
Petigura, E. A., Marcy, G. W., & Howard, A. W. 2013b, ApJ, 770, 69
Rogers, F. J., & Nayfonov, A. 2002, ApJ, 576, 1064
Rogers, L. A. 2014, in Proc. of IAU Symp., Vol. 299, Exploring the Formation and Evolution of Planetary Systems, ed. M. Booth, B. C. Matthews, & J. R. Graham (Cambridge: Cambridge Univ. Press), 247
Rowe, J. F., Bryson, S. T., Marcy, G. W., et al. 2014, ApJ, 784, 45
Roxburgh, I. W., & Vorontsov, S. V. 2003, A&A, 411, 215
Sanchis-Ojeda, R., Rappaport, S., Winn, J. N., et al. 2013, ApJ, 774, 54
Seager, S. 2010, Exoplanet Atmospheres: Physical Processes (Princeton, NJ: Princeton Univ. Press)
Seager, S., & Mallén-Ornelas, G. 2003, ApJ, 585, 1038
Silva Aguirre, V., Ballot, J., Serenelli, A. M., & Weiss, A. 2011, A&A, 529, A63
Silva Aguirre, V., Basu, S., Brandão, I. M., et al. 2013, ApJ, 769, 141
Smith, J. C., Stumpe, M. C., Van Cleve, J. E., et al. 2012, PASP, 124, 1000

Sozzetti, A., Torres, G., Charbonneau, D., et al. 2007, ApJ, 664, 1190
Steffen, J. H., Fabrycky, D. C., Ford, E. B., et al. 2012, MNRAS, 421, 2342
Stevenson, K. B., Harrington, J., Fortney, J. J., et al. 2012, ApJ, 754, 136
Stumpe, M. C., Smith, J. C., Van Cleve, J. E., et al. 2012, PASP, 124, 985
Swift, J. J., Johnson, J. A., Morton, T. D., et al. 2013, ApJ, 764, 105
Tegmark, M., Strauss, M. A., Blanton, M. R., et al. 2004, PhRvD, 69, 103501
Thoul, A. A., Bahcall, J. N., & Loeb, A. 1994, ApJ, 421, 828
Torres, G., Fischer, D. A., Sozzetti, A., et al. 2012, ApJ, 757, 161
Torres, G., Konacki, M., Sasselov, D. D., & Jha, S. 2004, ApJ, 614, 979

Torres, G., Winn, J. N., & Holman, M. J. 2008, ApJ, 677, 1324
Van Eylen, V., Lund, M. N., Silva Aguirre, V., et al. 2014, ApJ, 782, 14
Weiss, A., & Schlattl, H. 2008, Ap&SS, 316, 99
Winn, J. N., Johnson, J. A., Albrecht, S., et al. 2009, ApJL, 703, L99
Woitaszek, M., Metcalfe, T., & Shorrock, I. 2009, in Proc. 5th Grid Computing
    Environments Workshop, ed. J. Brown (New York: ACM), 1
Yoder, C. F. 1995, in Global Earth Physics: A Handbook of Physical Constants,
    ed. T. J. Ahrens (Washington, DC: American Geophysical Union), 1
Zeng, L., & Sasselov, D. 2013, PASP, 125, 227